

Accelerating High-Order Stencils on GPUs

Ryuichi Sai
Department of Computer Science
Rice University
Houston, TX, USA
ryuichi@rice.edu

John Mellor-Crummey
Department of Computer Science
Rice University
Houston, TX, USA
johnmc@rice.edu

Xiaozhu Meng
Department of Computer Science
Rice University
Houston, TX, USA
xm13@rice.edu

Mauricio Araya-Polo
Computational Science and Engineering
Total E&P Research and Technology US, LLC.
Houston, TX, USA

Jie Meng
Computational Science and Engineering
Total E&P Research and Technology US, LLC.
Houston, TX, USA

Abstract—Stencil computations are widely used in HPC applications. Today, many HPC platforms use GPUs as accelerators. As a result, understanding how to perform stencil computations fast on GPUs is important. While implementation strategies for low-order stencils on GPUs have been well-studied in the literature, not all of the techniques work well for high-order stencils, such as those used for seismic imaging. Furthermore, coping with boundary conditions often requires different computational logic, which complicates efficient exploitation of the thread-level parallelism on GPUs. In this paper, we study practical seismic imaging computations on GPUs using high-order stencils on large domains with meaningful boundary conditions. We manually crafted a collection of implementations of a 25-point seismic modeling stencil in CUDA along with code to apply the boundary conditions. We evaluated our stencil code shapes, memory hierarchy usage, data-fetching patterns, and other performance attributes. We conducted an empirical evaluation of these stencils using several mature and emerging tools and discuss our quantitative findings. Among our implementations, we achieve twice the performance of a proprietary code developed in C and mapped to GPUs using OpenACC. Additionally, several of our implementations have excellent performance portability.

Index Terms—stencil computation, high-order, boundary condition, HPC, GPU

I. INTRODUCTION

“Remember that Time is Money.” [1] This is even more true in today’s competitive business environments, such as the oil and gas industry, where fast simulations enable more realizations of experiments that can reduce the uncertainty of hydrocarbon reserves location or CO₂ storage management processes. Seismic depth imaging is the main tool used to extract information from seismic field records to identify relevant subsurface structures. High-order stencil computations typically serve as the foundation for seismic depth imaging. Over the past two decades, the availability of sufficiently powerful computational resources has led to the every-day use of more complex stencil-based wave equation approximations, and the power of today’s petascale systems enables simulations based on the full-wave equation instead of simple approximations.

Today, HPC platforms often employ Graphics Processing Units (GPUs) to increase their computational power. Accord-

ingly, using GPUs to accelerate full-wave equation simulations based on high-order stencils is a natural approach. However, the complexity of GPU architectures makes achieving top performance with high-order stencil computations surprisingly difficult. Without careful design, a stencil computation on a GPU is likely to underperform. An efficient implementation of high-order stencils with boundary conditions on a GPU requires paying careful attention to data reuse, warp utilization, work balance, and arithmetic intensity among other issues. For that reason, understanding how to develop efficient high-order stencils for GPUs is a topic of significant interest.

Since GPUs from different vendors have different characteristics and the characteristics of GPUs from a single vendor often change significantly between generations, performance portability across GPUs with varying characteristics is of significant interest. The best kernel on one GPU may not be the best on GPUs from other vendors and may not remain the best on newer generations of GPUs.

For these reasons, our current goal is to identify how to achieve excellent performance for high-order stencils on GPUs, and understand the factors that affect performance portability. To do so, we need to understand the strengths and weaknesses of various code shapes for high-order stencils. This paper describes our progress toward this goal and makes the following contributions:

- a careful comparison of existing approaches, including an assessment of their strengths and weaknesses when applied to high-order stencils with boundary conditions;
- the implementation and tuning of a collection of high-order stencil kernels with a selected set of algorithms and their variants using CUDA;
- a performance comparison of stencil implementations across multiple generations of NVIDIA GPUs along with a quantitative assessment of their performance using a Roofline performance model for GPUs; and
- an investigation of the characteristics of different stencil kernels that affect their performance

The next section is an overview of related work. Sections

III and IV present our approaches and implementations, respectively. Section V describes our evaluation methodology, experimental results, and a discussion of our findings. Section VI summarizes our conclusions and briefly discusses our plans for future work.

II. RELATED WORK

There is a rich literature describing efforts to efficiently implement stencil computations on CPUs [2], [3], [4], [5], [6], [7], [8], [9], [10], [11], [15], [16], [12] and GPUs [13], [14], [17], [18], [19], [22], [23]. We discuss the most related efforts below.

Time skewing [7], [8] accelerates stencil computations by increasing data reuse and cache locality by skewing one or more data dimensions by the time dimension so that several time steps can be computed for a tile while values are in cache. It has been widely used on CPUs, e.g., [9], [10], and [11].

Overlapped tiling uses time skewing to increase the arithmetic intensity of parallel stencil computations by trading redundant computation along the boundaries of overlapped tiles for a reduction in memory bandwidth required [12], [13]. Overlapped tiling is effective on GPUs because loading data from a GPU's global memory is much more costly than data-parallel computation. Furthermore, redundant computation can be overlapped with data accesses to help hide memory latency. While overlapped tiling has been shown to improve the performance of low-order stencils on GPUs, for high-order stencils, redundant computation grows quickly when skewed across multiple time steps by the width of a high-order stencil.

Split tiling [14] is an alternate approach for accelerating computation with time skewing. Rather than using overlapped tiles, which can introduce large amounts of redundant computation, split tiling computes points in two phases. The first phase computes tiles in parallel as hypertrapezoids that taper along the time dimension. Once all tiles from the first phase have been computed, a second phase back-fills the missing points in the time dimension.

The semi-stencil algorithm [15], [16], which has only been studied on CPUs, factors the computation of a stencil into two or more pieces. Rather than computing the result for a point as a single computation, the semi-stencil algorithm divides computation along one or more axes into two halves. While sweeping along a dimension, it computes the final result for one point and a partial result for another point a half-stencil width ahead. Compared to the traditional implementation of stencils, this approach changes the load/store ratio for the computation by trading half of the loads along a dimension for a store and a reload of a partial result. On a GPU, this has the potential for nearly halving the cache footprint of a thread block for a high-order stencil.

Nguyen et al. [17] introduce a 3.5D blocking algorithm as a mix of 2.5D spatial blocking with 1D temporal blocking. 2.5D spatial blocking involves blocking in a 2D plane and streaming along a third dimension. To increase data reuse, they store active 2D planes in GPU shared memory. In a 3.5D variant, they employ time skewing to advance the computation for multiple

time steps before writing data back to the global memory. While the 3.5D algorithm works very well on CPUs, the 1D temporal blocking introduces two potential implementation challenges for high-order stencils with boundary conditions on GPUs: barrier synchronizations and limited parallelism. In this paper, we evaluate 2.5D spatial blocking of high-order stencils and plan to explore 3.5D blocking in future work.

Nguyen et al.'s approach [17] loads a central plane along with halo planes above and below into shared memory for faster data access while computing stencil operations for points in the central plane. While this strategy improves data reuse, the size of a data tile is limited by the GPU shared memory size. To reduce the shared memory pressure, we looked into the work that uses registers on GPUs. Micikevicius [18] also uses 2.5D blocking; however, his approach maintains data points along the third dimension in registers rather than in shared memory.

Recently, as part of their AN5D framework work, Matsumura et al. [19] apply three more refinements to 2.5D and 3.5D solutions: fixed register allocations, double buffering, and division of the streaming dimension. While these approaches work extremely well for simple single-statement kernels, neither boundary conditions nor multi-statement stencils are evaluated. In our work, we study a high-order stencil with boundary conditions, and part of our application has multiple statements, instead of simple single-statement stencil updates.

Other interesting approaches to tackle the stencil computations including auto-tuning with dynamic resource allocations [20], DAG reordering [21], diamond tiling using polyhedral model [24], [25], functional programming [26], [27], and multi-layer intermediate representations [28], [29], [30].

From a software engineering perspective, there are two strategies for developing stencils for NVIDIA GPUs: hand-written kernels in CUDA and Domain-Specific Language (DSL)-based approaches [6], [22], [31], [32], [33], [34], [35]. The DSL approach can simplify the generation of code with complex logic. While we are interested in DSL-based approaches for the future, the focus of this paper is to understand in detail the strengths and weaknesses of various algorithmic strategies for achieving high performance and performance portability for high-order stencils. To avoid limitations as we explore this space, we chose to evaluate hand-written kernels.

III. APPROACH

We developed several implementations of the acoustic isotropic approximation of the wave equation [36] used for seismic imaging by the oil and gas industry. Solving this with finite differences involves using a high-order stencil-based solver with suitable boundary conditions. Oil and gas applications use such strategies on large grids to model subsurface and generate seismic data from source perturbations. In our work, we employ different code shapes that differ principally in how they organize the computation (e.g., 2D vs. 3D tiles) and how they manage the memory hierarchy. In the rest of this section, we will briefly describe the acoustic isotropic approximation, explain the various data decomposition strategies we employ,

<p>Data: \mathbf{f}: source Result: \mathbf{u}^n: wavefield at timestep n, for $n \leftarrow 1$ to T 1 $\mathbf{u}^0 := 0$; 2 for $n \leftarrow 1$ to T do 3 for each point in wavefield \mathbf{u}^n do 4 Solve Eq. 2 (left hand side) for wavefield \mathbf{u}^n; 5 end 6 $\mathbf{u}^n = \mathbf{u}^n + \mathbf{f}^n$ (Eq. 2 right hand side); 7 end</p>
--

Algorithm 1: A high-level description of the algorithm for solving the acoustic isotropic approximation of the wave equation with constant density.

describe blocking strategies, and discuss how we structure our implementations.

A. Seismic Modeling and Acoustic Isotropic Kernel

We study a stencil-based implementation of the acoustic isotropic wave equation approximation for seismic modeling. The details of the model are described in [36]. The wave equation for an acoustic isotropic operator with constant-density has the following form:

$$\frac{1}{\mathbf{V}^2} \frac{\partial^2 \mathbf{u}}{\partial t^2} - \nabla^2 \mathbf{u} = \mathbf{f}, \quad (1)$$

where $\mathbf{u} = \mathbf{u}(x, y, z)$ is the wavefield, \mathbf{V} is the Earth model (with velocity as rock property), and \mathbf{f} is the source perturbation. The equation is discretized in time using a second-order centered stencil, resulting in the semi-discretized equation:

$$\mathbf{u}^{n+1} - \mathbf{Q}\mathbf{u}^n + \mathbf{u}^{n-1} = (\Delta t^2) \mathbf{V}^2 \mathbf{f}^n, \text{ with } \mathbf{Q} = 2 + \Delta t^2 \mathbf{V}^2 \nabla^2. \quad (2)$$

Finally, the equation is discretized in space using a 25-point stencil in 3D, with eight points in along each axis surrounding a center point:

$$\begin{aligned} \nabla^2 \mathbf{u}(x, y, z) \approx & c_{xyz} \times \mathbf{u}(i, j, k) + \\ & \sum_{m=1}^4 c_{xm} \times [\mathbf{u}(i+m, j, k) + \mathbf{u}(i-m, j, k)] + \\ & c_{ym} \times [\mathbf{u}(i, j+m, k) + \mathbf{u}(i, j-m, k)] + \\ & c_{zm} \times [\mathbf{u}(i, j, k+m) + \mathbf{u}(i, j, k-m)] \end{aligned} \quad (3)$$

where $c_{xyz}, c_{xm}, c_{ym}, c_{zm}$ are the discretization parameters.

A high-level description of the algorithm is shown in Algorithm 1. We apply a Perfectly-Matched Layer (PML) [37] boundary condition to the regions around the physical domain. The resulting extended domain consists of an ‘‘inner’’ region where Equation (2) is applied, and the outer ‘‘boundary’’ region where a PML calculation is applied.

To solve the acoustic isotropic approximation for the wave equation, in the inner region we apply a complex multi-statement stencil that is 8th-order in space and 2nd-order in time. This involves applying a star shaped 25-point stencil to data stored in the u -array. In the PML layer, we employ a

7-point star shaped stencil to compute boundary conditions. The data for this 7-point stencil is stored in the eta -array.

In production simulations, the grid (that represent the physical domain) size is usually large (up to 4,000 grid points in each dimension). To yield results of practical use, the stencil computations need to be applied iteratively for a large number of time steps.

While we specifically study the acoustic isotropic kernel as the seismic model wave approximation in this paper, we believe that our approach is general enough that it could be applied to other high-order stencils with boundary conditions.

B. Data Domain Decomposition

As described in the previous section, our data domain contains two regions, the inner region and the Perfectly Matched Layer (PML) boundaries. The inner region is a cubic grid sits at the center of the data domain and the PML region represents the volume between the inner region and the data domain boundaries. The size of the inner region and the width of the PML region are defined as inputs to a simulation.

GPUs have different architectural characteristics than CPUs. As a result, GPU computations must be structured differently than CPU computations to achieve high performance. First, the Single-Instruction-Multiple-Thread (SIMT) execution model used by GPUs differs significantly from the execution model on CPUs. On NVIDIA GPUs, the execution model is realized by scheduling groups of 32 SIMT threads known as warps. To exploit thread-level parallelism in the SIMT model, GPU computations must utilize fine-grain data parallelism. A group of warps constitute a block which has its own quota for shared memory, registers, and other hardware resources; the number of blocks that can be active simultaneously is limited by the aggregated resource quota of active threads enforced by hardware limits. Second, since GPUs have a memory hierarchy distinct from CPUs, computations must be appropriately structured to exploit the GPU memory hierarchy. Finally, on NVIDIA GPUs, one could realize coarse-grain parallelism across Streaming Multiprocessors (SMs) by partitioning the computation into a sufficient number of blocks to keep the SMs busy.

We experimented with three decomposition strategies based on our data domain and boundary conditions.

First, we developed a single kernel that could be applied to any region of the data domain. The kernel contains conditionals that employ the PML calculations near any of the domain boundaries and compute the stencil for the acoustic isotropic wave function approximation in the inner region of the data domain. This strategy yields branch divergence for subregions that contain points in both the PML and inner regions which hurt performance.

Next, we developed separate kernels for the central region and the PML region. These separate kernels can be launched concurrently. This strategy eliminates the need for checking whether the point is inside inner region or PML region in every kernel, thus, reducing the chance of branch divergence. Nevertheless, it leaves unbalanced work among threads, along

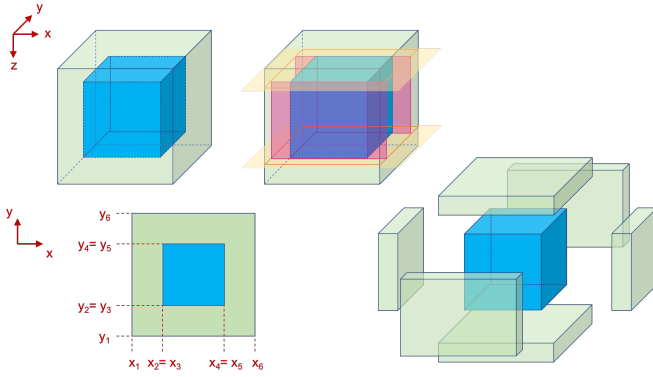


Fig. 1: Data Domain Decomposition

the boundaries between the inner and PML regions when the size of the GPU blocks doesn't evenly divide the extents of the PML and central regions.

Lastly, we developed the strategy as shown in Figure 1. We separate the inner region from PML region, and further divide PML region into six subregions. We slice the domain along the top and bottom of the inner region, and this gives us a top block, a bottom block, and a border of four walls. We further slice along the front and back, and it becomes four separate walls. These four walls and the two subregions from the first cuts result in total of six subregions of the PML region, namely: top, bottom, front, back, left and right subregions. The symmetry of these subregions is a relevant characteristic that we discuss later along with our results. Next, we launch individual GPU kernels of stencil computations for each of the seven subregions: one for the inner region and six for the PML subregions. This approach does not have intrinsic branch divergence at the boundaries. While there are still work imbalances due to different grid sizes, they occur only for a few edge cases along the borders. We could further reduce unbalanced work by using automated code generation that tailors the number of threads to match the number of points at border locations.

C. Blocking Strategies

For each of the seven regions, we further slice it into smaller blocks, so that each block can fit into GPU's resources for each kernel launch. We use two blocking strategies in our experiments: 3D Blocking and 2.5D Blocking.

1) *3D Blocking*: We divide each of the data regions into axis-aligned 3D blocks. To find the best block dimensions, we use fixed values in each execution to simplify experiments with different values. To perform stencil computations on GPUs, each block maps to a kernel launch with a 3D thread block with the thread dimensions matching the block dimensions. All points inside the block and their halos are explicitly copied into the GPU on-chip memory before any kernel is launched.

2) *2.5D Blocking*: We partition the data domain along the inner two X and Y data dimensions and perform a streaming computation along the outermost Z dimension. We launch

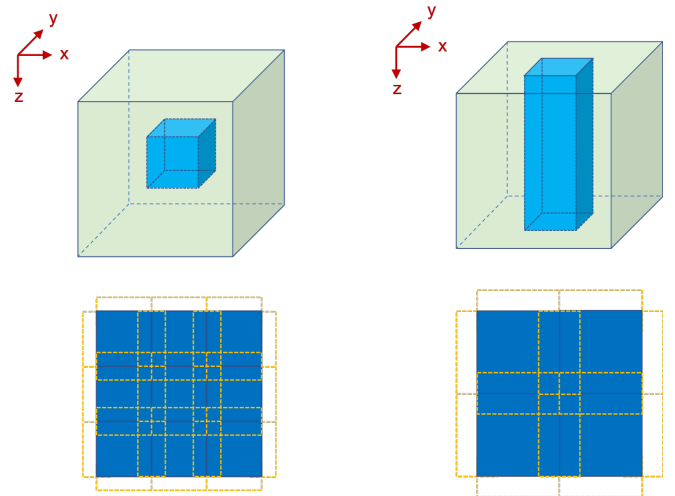


Fig. 2: Blocking Strategies: (left) 3D Blocking; (right) 2.5D Blocking

kernels with 2D thread blocks with their dimensions matching the 2D planes.

D. Kernels and their variants

We implemented several kernels. Each kernel employs a different combination of strategies for blocking, managing data accesses, and traversing the data volume. To better understand the strengths and weaknesses of these implementation alternatives, every implementation has multiple variants, which employ different tile sizes. We describe the details of our kernel implementations in the next section.

IV. IMPLEMENTATIONS

In describing our implementations, we use R to denote the width of the halo, which is half the spatial order of the stencil. For the acoustic isotropic simulations in our experiments, R is 4. Let N_x , N_y , and N_z denote the extents of the input data region along the X , Y , and Z axes, respectively. For 3D blocks, we use (x, y, z) to denote the 3D coordinate for both a point location in a 3D block and the thread in a kernel thread block. Similarly, for 2D planes, (x, y) is used to locate a point in the 2D plane, as well as identifying the thread.

1) *3D Blocking Using Global Memory Only*: This is conceptually and practically the simplest kernel to understand and implement. Let D_x , D_y , and D_z denote the block dimensions in the X , Y , and Z axes, respectively. Thus the block size is $D_x \times D_y \times D_z$. Because we launch each kernel with a thread block of the same size, the total number of points must be ≤ 1024 to respect the GPU limit of at most 1024 threads per block. The GPU grid size of each data region is $\lceil N_x/D_x \rceil \times \lceil N_y/D_y \rceil \times \lceil N_z/D_z \rceil$.

During execution of the 25-point stencil kernel, each thread fetches the point for itself, as well as 4 neighboring points along each direction of each axis. For good performance, we ensure a good memory access pattern when stencil points are fetched directly from global memory. Since we store the

3D grid data as a flat 1D array, we ensure global memory coalescing for the most innermost dimension X .

We refer to the family of 3D kernel implementations that fetch stencil points directly from the u array in global memory as $gmem_{\{Dx\}_{\{Dy\}_{\{Dz\}}$ in our experiments.

2) 3D Blocking Using Shared Memory for the u Array:

This approach is a variant of the aforementioned 3D blocking using global memory. It uses same 3D blocking strategy for each of the data regions; however, instead of computing directly on data fetched from global memory, this implementation fetches the u array from global memory, stores it into shared memory, and performs the stencil computation on data fetched from shared memory. The total number of points we fetch in this case is $Dx \times Dy \times Dz$ for a block and $(Dx \times Dy + Dx \times Dz + Dy \times Dz) \times R \times 2$ for halos around the block. For high order stencils, one must account for the halo size to ensure both the block and the halo fit in shared memory.

For high-order stencils, the halo accounts for a significant fraction of the data to fetch into shared memory. Thus, designing the right approach to minimize the fetch cost is crucial to overall performance. We describe the most general approach with good performance based on our experiments.

First, thread (i, j, k) fetches the point (i, j, k) . Then, when we design the block size, for each thread dimension, we must have at least $2R$ threads, and we use the first $2R$ threads along each dimension to fetch the halos. Along each dimension, threads 0 to $R - 1$ fetch the halo on one side, and threads R to $2R - 1$ fetch the halo on the other side. Fetching is perfectly balanced for each thread when $|D| = 2R$.

To use this strategy for the acoustic isotropic model where R is 4, we need to have at least eight threads along each dimension. Considering that maximum number of threads in a block is 1024 and the total amount of shared memory per block, the only possible tile size for this case is $8 \times 8 \times 8$. This results in perfectly balanced fetch work and computation for threads along each dimension.

Both the point and halo fetching need to be done in a fashion that enables global memory coalescing to the greatest extent possible.

We refer to the implementation that uses 3D blocking and shared memory as $smem_u$ in our experiments.

3) 3D Blocking Using Shared Memory for Boundary Regions: This implementation also exploits shared memory and uses 3D blocking. The main difference between this approach and the previous one is that this implementation fetches the eta array into shared memory, whereas the previous approach fetches the u array into shared memory. Because eta is only used in the stencil computation inside the PML region, this strategy applies only in the PML kernel.

This approach may appear to be nothing new; however, it is interesting for two reasons. First, as previously described, computations on eta in the PML region use a low-order 7-point stencil rather than the 25-point high-order stencil of the inner region. In fact, the halo size of eta is just one. Such low-order stencils have been widely studied in the literature;

however, the combination of high and low order stencils is seldom addressed. Second, this implementation gives us an opportunity to observe the performance changes by using global memory with a good access pattern for a high-order stencil, meanwhile using shared memory for a lower-order stencil.

In terms of fetching eta into shared memory, we have two implementations that differ in the number of conditionals. In our experiments, we refer to the shared memory kernel implementation that uses three conditionals as $smem_eta_3$ and the implementation that uses one conditional as $smem_eta_1$. We let R_eta denote the width of halos for eta , and for the acoustic isotropic PML layer, R_eta is 1.

$smem_eta_3$ uses an approach similar to $smem_u$, where the first $2R_eta$ threads from each dimension fetch the halos. Since we have three dimensions, we need three conditionals, one for each dimension, respectively. Because R_eta is just 1, we only need two threads fetching halos along each thread dimension. This could introduce unbalanced fetch work because for a 3D block of $8 \times 8 \times 8$, if only two threads in each dimension perform halo fetching, that is one fourth of the threads. Because we have three dimensions, only $1/64$ of the threads perform fetching, while others are idle.

<p>Data: $xidx, yidx, zidx$: thread index of x, y, and z dimension, respectively</p> <p>Data: nt: number of threads per block dimension</p> <p>Result: g: coordinate for global memory</p> <p>Result: s: coordinate for shared memory</p> <pre> 1 if $zidx < 6$ then 2 $z \leftarrow zidx \& 1$; 3 $sz \leftarrow z * 9$; 4 $gz \leftarrow z * (bt + 1) - 1$; 5 $xzswap \leftarrow zidx \leq 1$; 6 $yzswap \leftarrow (zidx \& 2) == 2$; 7 $si \leftarrow xzswap ? sz : (xidx + 1)$; 8 $sj \leftarrow yzswap ? sz : (yidx + 1)$; 9 $si \leftarrow xzswap ? (xidx + 1) : (yzswap ? (yidx + 1) : sz)$; 10 $gi \leftarrow xzswap ? gz : xidx$; 11 $gj \leftarrow yzswap ? gz : yidx$; 12 $gi \leftarrow xzswap ? xidx : (yzswap ? yidx : gz)$; 13 $s \leftarrow (si, sj, sk)$; 14 $g \leftarrow (gi, gj, gk)$; 15 end </pre>

Algorithm 2: Shared Memory Fetching Strategy for eta -array Using Only One Conditional

To address the work imbalance, we propose $smem_eta_1$ with only one condition, where we choose to use the first six threads from the X dimension to perform halo fetching. Algorithm 2 describes how we tilt the six planes of threads to identify the halo point that the each thread is responsible for the fetching. For $8 \times 8 \times 8$ 3D blocks, because $6/8$ threads perform the fetching, in theory, we reduce thread idleness to just 20%. However, this algorithm has relatively complex arithmetic to tilt each thread to its proper halo position, so an

experimental evaluation is needed to see whether the strategy is profitable.

4) *Semi-stencil*: Semi-stencil was initially introduced for CPUs, where it separates the stencil computations into two phases, namely the forward phase and the backward phase. The algorithm reads $R + 1$ points on one dimension, and the forward phases compute as the points are the left side of the stencil, and the partial result is stored to the rightmost point. Backward phases then compute as if the points are the right side of the stencil, and write out the final result to the leftmost point. By doing this, semi-stencil has the potential to improve performance by changing the ratio between load and store. For example, for a 3D stencil of halo size of R , with typical approach, it requires to load $6 * R + 1$ points in order to perform stencil computation for one point. Once the computation is done, a single store writes the result back. So the load-store-ratio is $(6 * R + 1) : 1$. On the other hand, using semi-stencil on one dimension, we read the center point and the half points with $R + 1$ loads, then forward phase writes one store, and backward phase write another store, thus total of two stores. Therefore, the load-store-ratio for semi-stencil is $(R + 1) : 2$. Also please note that, even for multi-dimensions, this ratio does not change. This is in theory very appealing for high-order stencils because the larger the size of the halo, the potential benefits one might achieve as the algorithm trades half of loads with just one more store. Therefore, we try to adopt semi-stencil algorithm on GPUs.

Our GPU implementation also uses 3D blocking. While the stencil computation in each 3D block is close to the CPU implementations described in the original paper. we further parallelize the executions by running all time steps concurrently on GPUs.

We assign the identifier *semi* to this implementation.

5) *2.5D Streaming with Multi-Plane using Shared Memory*: Starting from this implementation, we use 2.5D blocking. As already described, the 2.5D algorithm mainly streams a 2D plane through the third dimension. In our implementations, we choose the 2D XY-subplane because X is the innermost dimension in our data layout. Let Dx and Dy denote the dimensions of the 2D tile along the X and Y axes, respectively. So we launch kernels using 2D thread blocks with the size of Dx by Dy and a total of $Dx \times Dy$ threads. The GPU grid size of each data region is $\lceil Nx/Dx \rceil \times \lceil Ny/Dy \rceil$.

In this approach, we exploit shared memory as a buffer to store all data needed in the stencil computations for a particular XY-subplane. In addition to the current XY-subplane, we also load R subplanes above the current subplane and R subplanes below into the shared memory. Therefore, we allocate a buffer for $2R + 1$ planes, where each has $(Dx + 2R) \times (Dy + 2R)$ points, thus, total of $(2R + 1) \times (Dx + 2R) \times (Dy + 2R)$ points. Hence, the extent of each subplane must be carefully chosen so that the buffer size is as large as possible to enhance data reuse, but at the same time, it must be chosen so that the aggregate data volume of the planes doesn't exceed the shared memory available to a block. Let B denote our buffer, and $B[i]$ denote the i -th subplane in the buffer.

Before we can start the streaming computation, points from the top halos are pre-loaded into buffer $B[0..R)$ and the first R XY-subplanes are pre-loaded into $B[R..2R)$. Then, in our streaming loop, for each $z \leftarrow [0..Nz)$, we first load the $(z+R)$ -th XY-subplane into $B[(z + R) \bmod (2R + 1)]$; next, we perform the stencil computation for the z -th XY-subplane with the stencil points read from B in shared memory; finally, we store the result back to global memory.

While we explain this strategy using a modulus operator, in practice, we avoid using it for speed. Since the z index always increases by one inside the streaming loop, we use loop unrolling and index rotation to achieve the desired effect without modulus computations.

We refer to the family of kernel implementations of this strategy as $st_smem_ \{Dx\}_ \{Dy\}$ in our experiments.

The shared memory buffer used by this approach is limited by the GPU shared memory size. Alternatively, one can store data for stencil points along the streaming dimension in registers. We discuss two approaches that use registers to store points along the streaming dimension in the following sections.

6) *2.5D Streaming using Register Shifting*: In this 2.5D streaming approach, we keep points of the current XY-subplane in shared memory. However, when we stream along the z -axis, we use registers for the points along the z -axis. In contrast to shared memory, where data loaded from one thread is accessible by other threads in the same block, registers are only accessible by the current thread. Since we are streaming along the z -axis, the data from z -axis loaded for one thread is not needed by other threads.

So we allocate a shared memory space to hold $(Dx + 2R) \times (Dy + 2R)$ points for the currently active plane. The shared memory footprint compared to the previous method is $1 : (2R + 1)$. For high-order stencils, R is large so that the shared memory usage reduction is significant. Let $S(x, y)$ denotes the shared memory with location (x, y) .

We also allocate $2R + 1$ registers for the current point and its neighbors in each direction along the z -axis. Let $Reg(x, y)[i]$ denote the i -th register for the thread (x, y) .

Before we can start the streaming computation, thread (x, y) fetches data values from (x, y, z) for $z \leftarrow [-R..R)$ and stores them into register $Reg(x, y)[0..2R)$, respectively. Then, inside the stream loop, for each $z \leftarrow [0..Nz)$, we first shift the register indices back one position on each thread, such that for $r \leftarrow (0..2R)$, $Reg(x, y)[r - 1] = Reg(x, y)[r]$. Then, we load the leading point along the streaming dimension $(x, y, z + R)$ into register $Reg(x, y)[2R]$. Next, we fetch data (x, y, z) from global memory into $S(x, y)$; and we finally perform the stencil computation by using the data of XY-subplane from shared memory and data along the z -axis from registers. Finally, the kernel stores the stencil result for each thread back to global memory.

We refer to the family of kernel implementations using this strategy as $st_reg_shft_ \{Dx\}_ \{Dy\}$ in our experiments.

Although the notation we use above for registers might give the impression that we are using array indexing to access

register values, in our implementation, registers are expressed explicitly as $2R + 1$ scalar variables. Since our acoustic isotropic kernel has $R = 4$, which is the same as the sample code by Micikevicius [18], our implementation uses the same variable names: `behind4`, `behind3`, `behind2`, `behind1`, `current`, `front1`, `front2`, `front3`, and `front4`.

7) *2.5D Streaming using Fixed Registers with Loop Unrolling*: Like the previous approach, this implementation uses shared memory for the current XY-subplane and registers for points along the z-axis – the streaming dimension. However, the values in the registers are fixed instead of being “shifted.”

We again allocate a shared memory of $(Dx + 2R) \times (Dy + 2R)$ points. Let $S(x, y)$ denotes the shared memory for location (x, y) . We allocate $2R + 1$ registers as well, and denote $Reg(x, y)[i]$ for the i -th register of the thread (x, y) . In practice, they are $2R + 1$ named variables.

Before we can start the streaming computation, thread (x, y) fetches data from (x, y, z) for $z \leftarrow [-R..R]$ and stores them into register $Reg(x, y)[0..2R]$, respectively. Then, inside the stream loop, for each $z \leftarrow [0..Nz]$, we do not modify any value in the existing registers; we only update register $Reg(x, y)[(z + 2R) \bmod (2R + 1)]$ with the value of point $(x, y, z + R)$. Then, we fetch data (x, y, z) from global memory into $S(x, y)$. Next, we perform the stencil computation by using the data of XY-subplane from shared memory and i -th data above current point from $Reg(x, y)[(z + R - i) \bmod (2R + 1)]$, and j -th data below the current point from $Reg(x, y)[(z + R + j) \bmod (2R + 1)]$. Finally, the kernel stores the result back to global memory.

To further improve performance, we unroll the streaming loop. We introduce macros with register indices as macro placeholders. Inside the streaming loop, we expand $2R + 1$ macro calls, each with register indices shifted by one. We check and exit the loop when the stream reaches the boundary of z-axis.

We refer to the family of kernel implementations using this strategy as `st_reg_fixed_{Dx}_{Dy}` in our experiments.

V. EVALUATION

A. Experiment Environments

We evaluate all kernel implementations on three machines with NVIDIA GPUs across several generations. Table I lists our machine specifications. And we refer to the three machines by their GPU models.

- Machine `V100` is equipped with four NVIDIA V100 GPUs. We use one dedicated GPU for our experiments. We use the compiler option `-arch=sm_70` to compile all kernels for this platform.
- Machine `P100` is equipped with four NVIDIA P100 GPUs. We use one dedicated GPU for our experiments. We use the compiler option `-arch=sm_60` to compile all kernels for this platform.

	V100	P100	NVS510
CPU	IBM POWER9	IBM POWER8NVL	Intel Xeon E3-1245 v6
CPU Cores	160	160	8
RAM	256 GB	256 GB	16 GB
GPU	NVIDIA Tesla V100	NVIDIA Tesla P100	NVIDIA NVS 510
GRAM	32 GB	16 GB	2 GB
OS	RHEL v7.7	RHEL v7.4	Ubuntu 18.04 LTS
CUDA	10.2.89	10.1	10.2.89
NVIDIA Driver	440.33.01	418.39	440.33.01

TABLE I: Machine Specifications

- Machine `NVS510` has one NVIDIA NVS510 GPU. We use the compiler option `-arch=sm_30` to compile all kernels for this platform.

On `NVS510`, support for some tooling is marked as deprecated. While the tools work to some extent, many have limited functionality. Also, the GPU memory available on `NVS510` doesn’t support grid sizes needed for real-world use. Therefore, we only use this machine for basic comparisons across GPU generations. While we examine some metrics on this platform, we don’t discuss them in detail.

In most situations, we let the `nvcc` compiler figure out the register usage by itself, but we pay very close attention to the resulting register footprint. However, there are a few cases, where we specify the maximum number of registers used by a kernel using the compiler flag `-maxrregcount=X` to prevent register spilling.

We also use HPCToolkit [41], [42] version 20200803 and Empirical Roofline Toolkit [40]¹, and NVIDIA Nsight Compute version 2019.5.0 during our evaluations.

B. Evaluation Methodologies

We evaluate all implementations and their variants. First, we conduct basic time measurements. Second, we use HPCToolkit’s GPU support [42] to profile the kernel details with PC sampling. Third, we run Nsight Compute for device-specific kernel characteristics. Finally, we use the Empirical Roofline Toolkit to understand memory bandwidth limits on algorithm performance. We calculate the arithmetic intensity and the performance of every kernel, and compare them with the roofline chart. We describe each of our evaluation methods below.

1) *Time Measurements*: For each machine, based on its device memory size, we run the kernels with a large grid size supported by the device memory. For `V100`, we use a grid size of 1000^3 ; for `P100`, we use a grid size of 893^3 ; for `NVS510`, we use a grid size of 300^3 . As described in III-A, the stencil needs multiple iterations to converge. For benchmarking, we use 1000 iterations for all kernels on all machines. For each execution, we warm up the kernel by

¹We use a local fork of the tool for better Python 3 support and other minor changes needed for our environments. Our changes are made available at <https://github.com/rsrice/cs-roofline-toolkit-fork> under the same open-source license as the upstream repository <https://bitbucket.org/berkeleylab/cs-roofline-toolkit/src/master/>.

running the entire execution once, and then we repeat it five times, recording the average time for the five runs.

2) *HPCToolkit*: We use the August 2020 release of the HPCToolkit to collect GPU kernel metrics, such as register use, block and grid size, as well as PC sampling statistics such as exposed latencies and their kinds.

The evaluation contains four steps: Firstly, running `hpcrun` along with kernel executions for sampling using program counters. Thanks to the very low overhead of `hpcrun`, we can run our kernels with 1000 time iterations, which gives us accurate measurements that match the kernel behavior in the real world. Then, we use `hpcstruct` on the kernel binaries and recover the information about their relations to the source code. This is needed to contribute the performance metrics back to the source code, so that we can evaluate it later at the source code level, which makes the investigation easier. The source code structure computed by `hpcstruct` is then associated by `hpcprof` with the raw sampling data from `hpcrun`. Finally, a HPCToolkit performance database is generated.

HPCToolkit provides two graphical user interfaces to analyze the performance database, namely, `HPCViewer` and `HPCTraceViewer`. We use `HPCViewer` primarily for issues such as memory stalls, which enables us to easily spot which source lines have the most significant stalls. We also use `HPCViewer` to quickly identify the performance hotspots in our kernel executions using its code-centric views. We use `HPCTraceViewer` to inspect the program execution over time, which enables us to quickly spot idleness and see the associated calling contexts.

We describe some of our findings using HPCToolkit in our discussion of the evaluation results.

3) *Nsight Compute*: We run Nsight Compute for kernel characteristics, such as theoretical and achieved occupancy. Nsight Compute provides insights when performance differences are driven by the kernel characteristics. For example, when low occupancy happens, one can easily tell from an Nsight Compute report whether or not the problem seems to be associated with the register footprint, the shared memory footprint, or the number of threads.

Nsight Compute re-plays every kernel execution multiple times to collect a complete set of measurements, which adds a huge measurement overhead. When we use Nsight Compute, we run only five iterations.

4) *Roofline Performance Model*: We use the GPU Roofline performance model to see how well our kernels perform relative to a machine’s practical peak based on each kernel’s arithmetic intensity and the memory bandwidth-based performance limit for that particular arithmetic intensity.

We use the Empirical Roofline Toolkit (ERT) for machine characterizations. It runs several micro-benchmarks to characterize the peak compute speed and memory bandwidth of the machine. Benchmarking directly on a machine gives us an achievable performance bound, which is substantially lower than the theoretical peak claimed by the manufacturers when a kernel is memory bound.

We characterize kernels using `nvprof` by measuring several kernel performance metrics, including FLOPs, L2 read and write transactions, as well as DRAM read and write transactions. Output from `nvprof` is then fed into the calculations of both the performance and the arithmetic intensity for each kernel. Performance is calculated by the division of the measured FLOPs by the measured execution time. Arithmetic intensities are calculated by the division of the measured FLOPs by the measured bytes accessed on DRAM and L2 cache respectively.

We compare the performance of each kernel with the peak performance of the machine it runs on. We then compare kernels by their arithmetic intensities and their relative performance.

C. Results

In this section, we first present a summary of our results in tables and plots. After presenting our findings, we discuss our kernel measurements from several perspectives.

Table II presents time measurements for the kernels. For 3D blockings, the columns D_x , D_y , and D_z stand for the block dimensions along the x, y, and z axes, respectively. For 2.5D blockings, only columns for D_x and D_y are reported since the z-axis is unpartitioned. For Nr column, only values we explicitly specified are reported, and we use – for the ones that compiler decide.

Table III present the kernel characteristics for inner data region at the top, and PML regions at the bottom, respectively. As previous discussed, there are three symmetric groups for the PML subregions: top/bottom, front/back, and left/right. We group them in Table III. For shared characteristics across data regions, we further extract them into the `Static` column.

Table IV presents the performance characteristics of our implementations on the V100. Figure 3 visualizes these performance characteristics using roofline performance model, where Subfigures 3a and 3b showing the rooflines for L2 and DRAM, respectively, and Subfigures 3c and 3d are zoomed-in views the roofline kernel characteristics. The y-axes of these figures represent performance and x-axes show arithmetic intensity. The dots in each group of the implementations are categorized with the same color and their coordinates can be found in Table IV.

From our results, we offer the following observations.

3D Blocking using Global Memory:

The simplest implementation `gmem_8x8x8` using only the global memory yields the best performance on V100. With L1 data cache and shared memory combined into a single unified memory block on the V100 [43], we have a much larger data cache available on the V100 than on previous generations of GPUs. Therefore, when retrieving data from global memory with a good access pattern, we can achieve very good performance.

Comparing the performance of the 3D kernel across GPU generations, we notice its poor performance portability. It is one of the slowest implementations on P100 and the NVS510.

Kernel					Machine		
Kernel Identifier	Dx	Dy	Dz	Nr	V100	P100	NVS510
gmem_4x4x4	4	4	4	-	77.77	181.99	682.89
gmem_8x8x4	8	8	4	-	71.91	167.75	674.09
gmem_8x8x8	8	8	8	-	53.88	117.74	415.85
gmem_16x16x4	16	16	4	-	85.52	195.82	760.72
gmem_32x32x1	32	32	1	-	292.36	639.62	2507.22
smem_u	8	8	8	-	57.30	76.18	210.42
smem_eta_1	8	8	8	-	54.87	119.15	397.56
smem_eta_3	8	8	8	-	54.34	117.39	396.49
semi	8	8	8	-	172.84	217.29	1726.17
st_smem_8x8	8	8	-	-	116.38	112.71	509.18
st_smem_8x16	8	16	-	-	113.46	105.41	439.47
st_smem_16x8	16	8	-	-	59.92	77.91	425.73
st_smem_16x16	16	16	-	-	55.87	72.73	349.45
st_reg_shft_8x8	8	8	-	-	104.36	144.89	209.87
st_reg_shft_16x16	16	16	-	-	65.79	80.23	182.52
st_reg_shft_16x32	16	32	-	-	65.61	82.25	199.61
st_reg_shft_16x64	16	64	-	64	115.54	98.19	240.41
st_reg_shft_32x16	32	16	-	-	60.83	70.63	171.30
st_reg_shft_32x32	32	32	-	64	93.92	76.27	167.29
st_reg_shft_64x16	64	16	-	64	90.98	80.67	202.74
st_reg_fixed_8x8	8	8	-	-	113.88	152.75	195.05
st_reg_fixed_16x8	16	8	-	-	70.24	84.05	159.73
st_reg_fixed_16x16	16	16	-	-	61.66	76.10	170.03
st_reg_fixed_32x16	32	16	-	-	62.45	66.60	162.05
st_reg_fixed_32x32	32	32	-	64	58.96	61.74	160.91

TABLE II: Time Measurement

We tried several variants of the global memory implementation that differ each others in terms of block size, from smaller to larger, including `gmem_4x4x4`, `gmem_8x8x4`, `gmem_8x8x8`, `gmem_16x16x4`, and `gmem_32x32x1`. Our results show that, `gmem_8x8x8` is the best among them. We need to load all halos before performing stencil computations. For blocks smaller than `gmem_8x8x8`, such as `gmem_4x4x4` and `gmem_8x8x4`, the halo size for our 25-point stencil dominates the actual data points. Therefore, more time is spent on loading halos than points for the volume to be computed, which hurts performance. In addition, smaller block sizes also result in larger GPU grid size as we can see from Table III, which means more kernel launches. For the smaller blocks, the additional overheads slow the overall execution. On the other hand, we also see performance degradation for larger blocks, `gmem_16x16x4` and `gmem_32x32x1`. Their larger block size results in a smaller grid size. However, both have low theoretical and achieved occupancy. Table IV shows that the 3D kernels using larger blocks, especially `gmem_32x32x1`, incur more L2 cache misses, which increases the number of high-latency loads from global memory.

In summary, the global memory implementations are the simplest to program and need very little performance tuning. With the right tile shape and using a good global memory access pattern, on late-model GPU architectures, such as V100, one can achieve amazingly good performance with little effort. From a software engineering perspective, these implementations are easy to understand and have a low maintenance cost.

Shared memory:

Table II shows that using shared memory can boost performance. The yield performance gain is more significant on older generation GPUs, such as P100 and NVS510, which is consistent with results in previous research.

Recall that `smem_u` is a high-order stencil while `smem_eta_1` and `smem_eta_3` are not. From Table II, we saw `smem_u` runs faster than `smem_eta_1` and `smem_eta_3` on V100, but oppositely, it is slower on P100 and NVS510. We attribute this conflicting results to the architectural changes in V100, where it combines the L1 data cache with shared memory. As discussed previously, on V100, with good access patterns for global memory, one can achieve great performance with little effort. The overhead of using shared memory on V100 in 3D blocking erases this gain. In contrast, older generation GPUs do not have this new feature, so shared memory provides more performance benefits than its overhead. On older architectures, with high-order stencils, such as `smem_u`, because we load larger-size blocks into shared memory than low-order ones, such as `smem_eta_1` and `smem_eta_3`, we see better performance.

For high-order stencils, which have a large halo size, it is not hard to reach the shared memory limit. While shared memory improves performance, the hardware limitation on shared memory limits the potential of holding all data on shared memory for high-order stencils which use large blocks.

Semi-stencil:

Thread synchronizations on GPUs are very expensive, and our evaluations also prove so with our semi-stencil implementation. Because of the need of storing and loading partial results, thread synchronizations are necessary to ensure the

Kernel Identifier	Block Size	Grid Size	Registers Per Thread	Achieved Active Warps	Achieved Occupancy	Theoretical Active Warps	Theoretical Occupancy
gmem_4x4x4	64	13,312,053	40	37.2	58.2	48.0	75.0
gmem_8x8x4	256	3,356,157	40	44.0	68.7	48.0	75.0
gmem_8x8x8	512	1,685,159	40	42.5	66.4	48.0	75.0
gmem_16x16x4	1,024	853,200	40	28.9	45.2	32.0	50.0
gmem_32x32x1	1,024	851,400	40	29.3	45.8	32.0	50.0
smem_u	512	1,685,159	38	44.6	69.7	48.0	75.0
smem_eta_1	512	1,685,159	40	42.4	66.3	48.0	75.0
smem_eta_3	512	1,685,159	40	42.4	66.2	48.0	75.0
semi	768	1,685,159	40	41.2	64.4	48.0	75.0
st_smem_8x8	64	14,161	56	19.9	31.1	20.0	31.2
st_smem_8x16	128	7,140	56	27.9	43.6	28.0	43.7
st_smem_16x8	128	7,140	56	27.9	43.5	28.0	43.7
st_smem_16x16	256	3,600	56	31.6	49.4	32.0	50.0
st_reg_shft_8x8	64	14,161	96	19.0	29.7	20.0	31.2
st_reg_shft_16x16	256	3,600	96	15.9	24.9	16.0	25.0
st_reg_shft_16x32	512	1,800	96	16.0	25.0	16.0	25.0
st_reg_shft_16x64	1,024	900	64	32.0	50.0	32.0	50.0
st_reg_shft_32x16	512	1,800	96	16.0	25.0	16.0	25.0
st_reg_shft_32x32	1,024	900	64	32.0	50.0	32.0	50.0
st_reg_shft_64x16	1,024	900	64	32.0	50.0	32.0	50.0
st_ref_fixed_8x8	64	14,161	78	23.9	37.3	24.0	37.5
st_ref_fixed_16x8	128	7,140	78	23.9	37.3	24.0	37.5
st_ref_fixed_16x16	256	3,600	78	23.9	37.4	24.0	37.5
st_ref_fixed_32x16	512	1,800	78	16.0	25.0	16.0	25.0
st_ref_fixed_32x32	1,024	900	64	32.0	50.0	32.0	50.0

Kernel Identifier	Static				Top/Bottom			Front/Back			Left/Right		
	Block Size	Registers Per Thread	Theoretical Active Warps	Theoretical Occupancy	Grid Size	Achieved Active Warps	Achieved Occupancy	Grid Size	Achieved Active Warps	Achieved Occupancy	Grid Size	Achieved Active Warps	Achieved Occupancy
gmem_4x4x4	64	48	40.0	62.5	437500	38.0	59.5	414750	38.0	59.4	393183	38.2	59.7
gmem_8x8x4	256	48	40.0	62.5	109375	37.5	58.6	118500	37.5	58.6	112812	36.7	57.3
gmem_8x8x8	512	48	32.0	50.0	62500	29.2	45.7	59500	26.9	42.0	56644	28.2	44.1
gmem_16x16x4	1024	48	32.0	50.0	27783	30.0	46.6	29862	29.5	46.1	28440	26.0	40.2
gmem_32x32x1	1024	48	32.0	50.0	27648	29.0	45.0	30272	29.0	45.0	28380	24.2	38.0
smem_u	512	48	32.0	50.0	62500	30.1	47.1	59500	27.8	43.5	56644	27.7	43.3
smem_eta_1	512	32	64.0	100.0	62500	59.4	92.9	59500	54.8	85.6	56644	54.8	85.7
smem_eta_3	512	32	64.0	100.0	62500	59.1	92.4	59500	53.9	84.3	56644	54.2	84.8
semi	768	64	24.0	37.5	62500	17.7	27.6	59500	18.7	29.3	56644	17.5	27.3
st_smem_8x8	64	72	20.0	31.2	500	12.4	19.4	476	11.8	18.5	14161	19.7	30.8
st_smem_8x16	128	72	28.0	43.7	252	12.6	19.7	238	11.8	18.5	7140	27.5	43.1
st_smem_16x8	128	72	28.0	43.7	250	12.4	19.5	240	11.9	18.6	7140	27.5	43.0
st_smem_16x16	256	72	24.0	37.5	126	12.7	19.8	120	12.0	18.7	3600	23.9	37.3
st_reg_shft_8x8	64	80	24.0	37.5	500	12.4	19.4	476	11.8	18.4	14161	23.6	36.8
st_reg_shft_16x16	256	80	24.0	37.5	126	12.6	19.7	120	11.9	18.6	3600	23.9	37.3
st_reg_shft_16x32	512	80	16.0	25.0	64	16.0	25.0	60	16.0	25.0	1800	15.9	24.9
st_reg_shft_16x64	1024	64	32.0	50.0	32	32.0	50.0	60	31.9	49.9	900	31.9	49.8
st_reg_shft_32x16	512	80	16.0	25.0	63	16.0	25.0	60	16.0	25.0	1800	15.9	24.9
st_reg_shft_32x32	1024	64	32.0	50.0	32	32.0	50.0	30	31.9	49.9	900	31.8	49.8
st_reg_shft_64x16	1024	64	32.0	50.0	63	31.9	49.9	30	31.9	49.9	900	31.8	49.8
st_ref_fixed_8x8	64	106	16.0	25.0	500	12.4	19.4	476	11.8	18.4	14161	15.7	24.6
st_ref_fixed_16x8	128	104	16.0	25.0	250	12.4	19.5	240	11.8	18.5	7140	15.7	24.6
st_ref_fixed_16x16	256	104	16.0	25.0	126	12.6	19.8	120	12.0	18.7	3600	15.8	24.7
st_ref_fixed_32x16	512	106	16.0	25.0	63	16.0	25.0	60	16.0	25.0	1800	15.9	24.9
st_ref_fixed_32x32	1024	64	32.0	50.0	32	32.0	50.0	30	31.9	49.9	900	31.9	49.8

TABLE III: Kernel Characteristics on V100: (top) Inner; (bottom) PML

completeness of the required computation before it can proceed to the next. As GPU runs threads concurrently in warps, we must introduce proper barriers to prevent data from being corrupted. Our choice of using 3D blocking requires thread synchronizations on all three dimensions, which exacerbates the problem. HPCToolkit also backs our reasoning with its second most significant bottleneck being the thread synchronization (STL_SYNC).

Nevertheless, the methodology behind semi-stencil algo-

rithm is still valid. Thus, to avoid the excess use of thread synchronizations, we will investigate into using double buffering. As well, we will explore using 2.5D blocking instead of 3D blocking in our future work.

Code Shape for 2.5D-Blockings:

For implementations using 2.5D-blocking, we observe the larger the 2D plane, the better the performance. There are

Kernel Identifier	FLOP (x10 ¹³)	Achieved Performance (GFLOPs)	L2 Transactions (x10 ¹²)	L2 Arithmetic Intensity	L2 Machine Peak Performance (GFLOPs)	L2 Achieved Percentage	DRAM Transactions (x10 ¹¹)	DRAM Arithmetic Intensity	DRAM Machine Peak Performance (GFLOPs)	DRAM Achieved Percentage
gmem_4x4x4_opt	4.453	533	3.38	0.41	1361	39.19%	8.42	1.65	1291	41.29%
gmem_8x8x4_opt	4.453	577	2.81	0.49	1635	35.27%	7.26	1.92	1498	38.50%
gmem_8x8x8_opt	4.453	770	1.79	0.78	2566	30.00%	7.26	1.92	1498	51.39%
gmem_16x16x4_opt	4.453	485	2.45	0.57	1877	25.83%	6.67	2.08	1628	29.78%
gmem_32x32x1_opt	4.453	142	13.90	0.10	330	42.95%	6.56	2.12	1656	8.57%
smem_u_opt	4.453	724	1.82	0.77	2531	28.60%	7.37	1.89	1474	49.11%
smem_eta_1_opt	4.453	756	1.82	0.76	2522	29.97%	7.31	1.90	1487	50.81%
smem_eta_3_opt	4.453	763	1.81	0.77	2535	30.10%	7.31	1.90	1488	51.30%
semi_opt	6.400	345	2.67	0.75	2480	13.90%	18.40	1.08	847	40.71%
st_smem_8x8_opt	4.453	356	1.59	0.87	2891	12.33%	12.30	1.13	885	40.27%
st_smem_8x16_opt	4.453	366	1.47	0.95	3130	11.68%	13.30	1.05	820	44.58%
st_smem_16x8_opt	4.453	692	1.17	1.19	3933	17.59%	7.74	1.80	1404	49.27%
st_smem_16x16_opt	4.453	742	1.04	1.34	4414	16.81%	6.97	2.00	1560	47.58%
st_reg_shft_8x8_opt	4.453	397	1.57	0.89	2935	13.54%	10.40	1.34	1047	37.96%
st_reg_shft_16x16_opt	4.453	630	1.20	1.16	3841	16.41%	7.22	1.93	1506	41.86%
st_reg_shft_16x32_opt	4.453	632	1.15	1.21	3991	15.84%	6.76	2.06	1607	39.32%
st_reg_shft_16x64_opt	4.453	359	1.99	0.70	2317	15.49%	17.00	0.82	638	56.25%
st_reg_shft_32x16_opt	4.453	682	0.94	1.47	4861	14.02%	6.94	2.00	1566	43.54%
st_reg_shft_32x32_opt	4.453	442	1.67	0.83	2750	16.05%	15.50	0.90	701	62.95%
st_reg_shft_64x16_opt	4.453	456	1.57	0.89	2938	15.52%	14.50	0.96	752	60.64%
st_reg_fixed_8x8_opt	4.453	364	1.65	0.84	2791	13.05%	15.00	0.93	723	50.36%
st_reg_fixed_16x8_opt	4.453	590	1.27	1.10	3632	16.26%	9.59	1.45	1133	52.11%
st_reg_fixed_16x16_opt	4.453	673	1.18	1.18	3899	17.25%	7.71	1.80	1409	47.72%
st_reg_fixed_32x16_opt	4.453	664	9.12	1.53	5043	13.17%	7.14	1.95	1522	43.62%
st_reg_fixed_32x32_opt	4.453	703	1.09	1.27	4209	16.71%	9.08	1.53	1197	58.78%

TABLE IV: Kernel Performance Characteristics on V100

two main reasons for this. First, a larger 2D plane means a higher degree of concurrency. Second, with a larger plane, the percentage of halo points fetched into shared memory is smaller, which speeds up the overall performance.

In addition, our results show that `st_reg_shft_32x16` runs faster than `st_reg_shft_16x32`. From Table IV, we see more L2 transactions with `st_reg_shft_16x32`, which in turn harms performance. Therefore, one should cut the plane so that the x-dimension of the GPU’s thread block assigned to the innermost dimension has a relatively larger size.

Register Footprint in 2.5D-Blockings:

When we evaluate `st_reg_shft_*` implementations, the variants with 2D plane size of 1024, namely `st_reg_shft_16x64`, `st_reg_shft_32x32`, and `st_reg_shft_64x16`, show poor performance on V100. The performance degradation is caused by register spilling. The maximum registers in a blockthread is $64 \times 1024 = 65536$. Because we have 1024 threads for these implementations, we can only have maximum 64 registers for each thread. If we do not explicitly specify the register count to `nvcc`, it assigns 80 and 96 registers to the PML and inner kernels, respectively. Running the generated binaries for these register footprints yields incorrect results. To avoid this problem, we use compiler flag `-maxrregcount=64` to limit the maximum register usage per thread. Unfortunately 64 registers are not enough to hold all of the variables at the same time, causing register spilling. The register shifting approach exacerbates register spilling due to its high frequency of register access.

However, although register spilling happens to the register shifting kernels, for the `st_fixed_reg_32x32` kernel, we don’t see a performance degradation because the code uses fixed registers with loop unrolling. Because the registers are fixed, the frequency of register data movement is smaller than for kernels using the register shifting approach. This allows the performance impacted by register spilling to be hidden by other thread activities.

GPU Warp Occupancies:

Table III shows implementations using 2.5D blocking in general have better theoretical and achieved occupancies than the ones using 3D blocking.

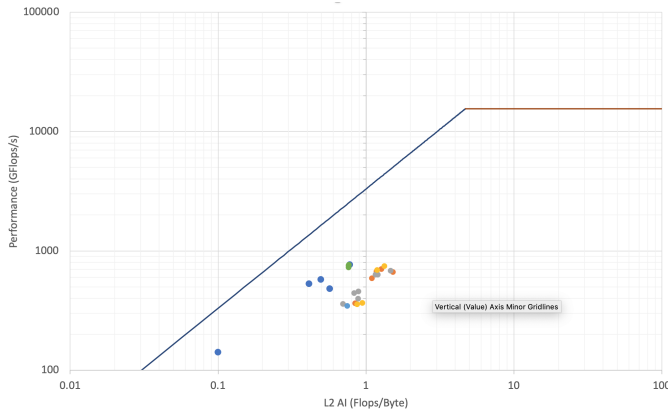
Performance Portability:

The best performing implementations on P100 and NVS510 come from 2.5D approaches. Although they are not the best kernels on V100, they are still in the fastest tier. Thus, if performance portability is a concern, implementations using 2.5D blocking, such as `st_reg_fixed_32x32`, would be preferred.

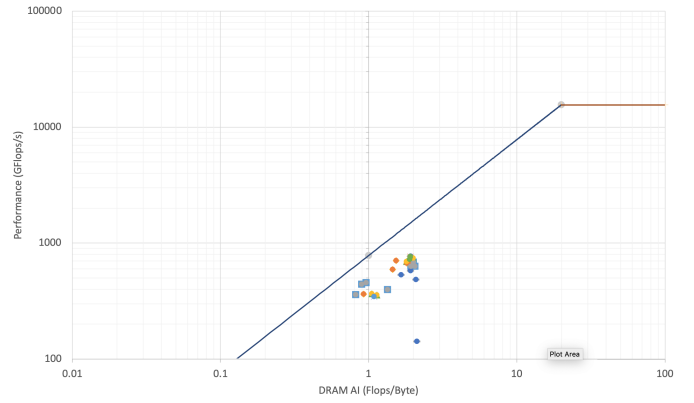
Gaps to the Roofline Ceilings:

Our interpretation of the performance gaps are twofold:

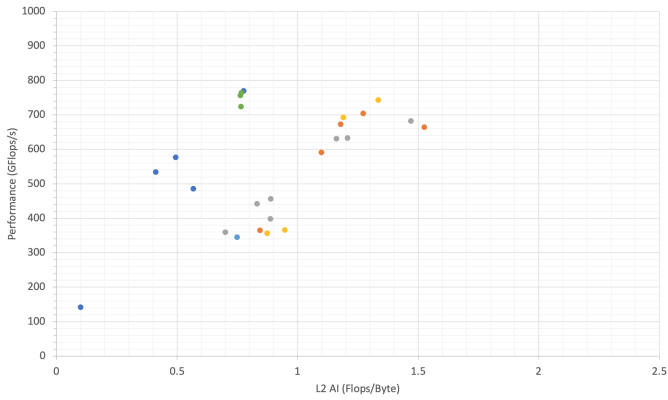
First, although our current implementations realize a good performance for high-order stencils with boundary conditions, we see room for further performance tuning. We could improve the arithmetic intensities by designing new GPU code shapes, e.g., by employing the semi-stencil algorithm [15], [16], which reduces data movement for high-order stencils,



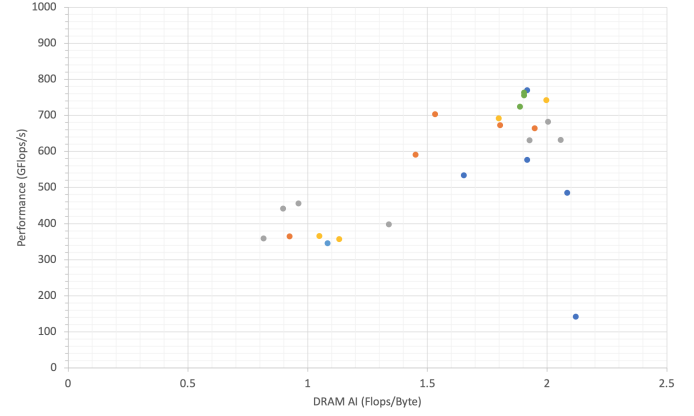
(a) Device Performance vs L2 Arithmetic Intensity



(b) Device Performance vs DRAM Arithmetic Intensity



(c) Kernel Performance vs L2 Arithmetic Intensity



(d) Kernel Performance vs DRAM Arithmetic Intensity

● gmem ● st_reg_fixed ● st_reg_shift ● st_smem ● semi ● smem

Fig. 3: Roofline Performance on V100

or employing time-skewing to increase data reuse. While all of our implementations were manually written in CUDA, we could develop a new DSL approach or build a framework that enables us to explore more sophisticated approaches.

Second, ERT uses simple micro-benchmarks to profile the machines. In contrast, the acoustic isotropic model not only uses high-order stencils with complex boundary conditions, but also contains complicated logic with multiple statements. Thus, while the roofline ceilings provide us a guide, the logic of our complex kernels makes it difficult to hit the roofline limit.

VI. CONCLUSIONS AND FUTURE WORK

In this paper, we evaluated the performance of high-order stencils with boundary conditions. We reviewed the existing techniques for implementing 3D stencil computations and evaluated most of them suitable for high-order stencils, with the notable exception of time-skewing algorithms. We implemented multiple versions of different approaches using known techniques and combinations of them, modifying approaches as needed to better accommodate high-order stencils with

boundary conditions. We evaluated our implementations with several tools on multiple platforms, quantitatively comparing stencils from various perspectives, and presented our findings and observations.

We began our evaluation by computing 25-point stencil algorithms over the entire data domain in a single kernel launch. Inefficiency caused by branch divergence led us to apply domain decomposition and compute the boundaries separate from the center region. While this improved efficiency, having the regions separate impedes our ability to apply time skewing along the streaming dimension for the 2.5D algorithm. We plan to reintegrate boundary computations with the inner region to enable us to evaluate 3.5D algorithms on high-order stencils by adding time skewing to the streaming dimension. In addition, we would like to explore whether applying the semi-stencil algorithm [15] along the streaming dimension to reduce the memory hierarchy footprint of a block's stencil calculations and increase the arithmetic intensity of high-order kernels. We plan to experiment with the range of kernels on the NVIDIA A100 GPU to assess performance portability. In addition to NVIDIA GPUs, we plan to expand the scope of

our evaluation to explore the performance of various high-order stencil implementations on leading-edge GPUs from other vendors, as soon as we can gain access to them and results on them are not embargoed.

We recognize that implementing, tuning, maintaining, and porting high-performance GPU kernels for high-order stencils is quite difficult. For the long term, we believe that a high-level representation of stencil computations in conjunction with powerful compiler technology is arguably the best strategy to improve development productivity and performance portability while also lowering maintenance costs by reducing complexity. However, a concern for DSL users is the long-term viability of their code. We are hopeful that adding DSL technology to the LLVM compiler framework will provide a path forward that will address this concern.

ACKNOWLEDGMENT

This work was supported in part by a contract from Total E&P Research & Technology USA, LLC. We thank Keren Zhou from Rice University for reviewing the drafts of this paper and helping us use his emerging GPU Performance Advisor tool, which offered insights for tuning some of the kernels we studied.

REFERENCES

- [1] F. Benjamin, "Advice to a Young Tradesman," National Archives and Records Administration/University of Virginia Press, July 1748.
- [2] M. Frigo, C. E. Leiserson, H. Prokop, and S. Ramachandran, "Cache-Oblivious Algorithms," in Proceedings of the 40th Annual Symposium on Foundations of Computer Science, USA, Oct. 1999, p. 285.
- [3] M. Frigo and V. Strumpen, "Cache oblivious stencil computations," in Proceedings of the 19th annual international conference on Supercomputing, Cambridge, Massachusetts, Jun. 2005, pp. 361-366.
- [4] M. Frigo and V. Strumpen, "The cache complexity of multithreaded cache oblivious algorithms," in Proceedings of the eighteenth annual ACM symposium on Parallelism in algorithms and architectures, Cambridge, Massachusetts, USA, Jul. 2006, pp. 271-280.
- [5] R. Strzodka, M. Shaheen, D. Pajak, and H.-P. Seidel, "Cache oblivious parallelograms in iterative stencil computations," in Proceedings of the 24th ACM International Conference on Supercomputing, Tsukuba, Ibaraki, Japan, Jun. 2010, pp. 49-59.
- [6] Y. Tang, R. A. Chowdhury, B. C. Kuzmaul, C.-K. Luk, and C. E. Leiserson, "The pochoir stencil compiler," in Proceedings of the twenty-third annual ACM symposium on Parallelism in algorithms and architectures, San Jose, California, USA, Jun. 2011, pp. 117-128.
- [7] D. Wonnacott, "Using time skewing to eliminate idle time due to memory bandwidth and network limitations," in Proceedings 14th International Parallel and Distributed Processing Symposium. IPDPS 2000, May 2000, pp. 171-180.
- [8] D. Wonnacott, "Achieving Scalable Locality with Time Skewing," International Journal of Parallel Programming, vol. 30, no. 3, pp. 181-221, Jun. 2002.
- [9] G. Jin, J. Mellor-Crummey, and R. Fowler, "Increasing Temporal Locality with Skewing and Recursive Blocking," in SC01: Proceedings of the 2001 ACM/IEEE Conference on Supercomputing, Nov. 2001, pp. 57.
- [10] J. McCalpin and D. Wonnacott, "Time Skewing: A Value-Based Approach to Optimizing for Memory Locality," 1998.
- [11] Y. Song and Z. Li, "New tiling techniques to improve cache temporal locality," SIGPLAN Not., vol. 34, no. 5, pp. 215-228, May 1999.
- [12] S. Krishnamoorthy, M. Baskaran, U. Bondhugula, J. Ramanujam, A. Rountev, and P. Sadayappan, "Effective automatic parallelization of stencil computations," SIGPLAN Not., vol. 42, no. 6, pp. 235-244, Jun. 2007.
- [13] J. Holewinski, L.-N. Pouchet, and P. Sadayappan, "High-performance code generation for stencil computations on GPU architectures," in Proceedings of the 26th ACM international conference on Supercomputing, San Servolo Island, Venice, Italy, Jun. 2012, pp. 311-320.
- [14] T. Grosser, A. Cohen, P. H. J. Kelly, J. Ramanujam, P. Sadayappan, and S. Verdoolaege, "Split tiling for GPUs: automatic parallelization using trapezoidal tiles," in Proceedings of the 6th Workshop on General Purpose Processor Using Graphics Processing Units, Houston, Texas, USA, Mar. 2013, pp. 24-31.
- [15] R. de la Cruz, M. Araya-Polo, and J. M. Cela, "Introducing the Semi-stencil Algorithm," in Parallel Processing and Applied Mathematics, Berlin, Heidelberg, 2010, pp. 496-506.
- [16] R. de la Cruz and M. Araya-Polo, "Algorithm 942: Semi-Stencil," ACM Trans. Math. Softw., vol. 40, no. 3, p. 23:1-23:39, Apr. 2014.
- [17] A. Nguyen, N. Satish, J. Chhugani, C. Kim, and P. Dubey, "3.5-D Blocking Optimization for Stencil Computations on Modern CPUs and GPUs," in SC 10: Proceedings of the 2010 ACM/IEEE International Conference for High Performance Computing, Networking, Storage and Analysis, Nov. 2010, pp. 1-13.
- [18] P. Micikevicius, "3D finite difference computation on GPUs using CUDA," in Proceedings of 2nd Workshop on General Purpose Processing on Graphics Processing Units, Washington, D.C., USA, Mar. 2009, pp. 79-84.
- [19] K. Matsumura, H. R. Zohouri, M. Wahib, T. Endo, and S. Matsuoka, "AN5D: automated stencil framework for high-degree temporal blocking on GPUs," in Proceedings of the 18th ACM/IEEE International Symposium on Code Generation and Optimization, San Diego, CA, USA, Feb. 2020, pp. 199-211.
- [20] P. S. Rawat, M. Vaidya, A. Sukumaran-Rajam, A. Rountev, L.-N. Pouchet, and P. Sadayappan, "On Optimizing Complex Stencils on GPUs," in 2019 IEEE International Parallel and Distributed Processing Symposium (IPDPS), May 2019, pp. 641-652.
- [21] P. S. Rawat, F. Rastello, A. Sukumaran-Rajam, L.-N. Pouchet, A. Rountev, and P. Sadayappan, "Register optimizations for stencils on GPUs," SIGPLAN Not., vol. 53, no. 1, pp. 168-182, Feb. 2018.
- [22] P. Rawat et al., "SDSLc: a multi-target domain-specific compiler for stencil computations," in Proceedings of the 5th International Workshop on Domain-Specific Languages and High-Level Frameworks for High Performance Computing, Austin, Texas, Nov. 2015, pp. 1-10.
- [23] P. S. Rawat et al., "Domain-Specific Optimization and Generation of High-Performance GPU Code for Stencil Computations," Proceedings of the IEEE, vol. 106, no. 11, pp. 1902-1920, Nov. 2018.
- [24] U. Bondhugula, A. Hartono, J. Ramanujam, and P. Sadayappan, "A practical automatic polyhedral parallelizer and locality optimizer," SIGPLAN Not., vol. 43, no. 6, pp. 101-113, Jun. 2008.
- [25] V. Bandishti, I. Pananilath, and U. Bondhugula, "Tiling stencil computations to maximize parallelism," in SC 12: Proceedings of the International Conference on High Performance Computing, Networking, Storage and Analysis, Nov. 2012, pp. 1-11.
- [26] M. Steuwer, T. Rimmelg, and C. Dubach, "LIFT: A functional data-parallel IR for high-performance GPU code generation," in 2017 IEEE/ACM International Symposium on Code Generation and Optimization (CGO), Feb. 2017, pp. 74-85.
- [27] M. L?cke, M. Steuwer, and A. Smith, "A functional pattern-based language in mlir," p. 6, 2020.
- [28] O. Fuhrer et al., "Towards a performance portable, architecture agnostic implementation strategy for weather and climate models," Supercomput. Front. Innov.: Int. J., vol. 1, no. 1, pp. 45-62, Apr. 2014.
- [29] J.-M. Gorius and T. Grosser, "Modeling Stencils in a Multi-Level Intermediate Representation," p. 15, 2019.
- [30] T. Gysi et al., "Domain-Specific Multi-Level IR Rewriting for GPU," arXiv:2005.13014 [cs], May 2020, Accessed: Jul. 19, 2020. [Online]. Available: <http://arxiv.org/abs/2005.13014>.
- [31] R. Baghdadi et al., "PENCIL: A Platform-Neutral Compute Intermediate Language for Accelerator Programming," in 2015 International Conference on Parallel Architecture and Compilation (PACT), Oct. 2015, pp. 138-149.
- [32] R. Baghdadi et al., "Tiramisu: a polyhedral compiler for expressing fast and portable code," in Proceedings of the 2019 IEEE/ACM International Symposium on Code Generation and Optimization, Washington, DC, USA, Feb. 2019, pp. 193-205, Accessed: Jul. 20, 2020. [Online].
- [33] M. Christen, O. Schenk, and H. Burkhardt, "PATUS: A Code Generation and Autotuning Framework for Parallel Iterative Stencil Computations on Modern Microarchitectures," in 2011 IEEE International Parallel Distributed Processing Symposium, May 2011, pp. 676-687.
- [34] M. Louboutin et al., "Devito (v3.1.0): an embedded domain-specific language for finite differences and geophysical exploration," Geoscientific Model Development, vol. 12, no. 3, pp. 1165-1187, Mar. 2019.

- [35] J. Ragan-Kelley, C. Barnes, A. Adams, S. Paris, F. Durand, and S. Amarasinghe, "Halide: a language and compiler for optimizing parallelism, locality, and recomputation in image processing pipelines," in Proceedings of the 34th ACM SIGPLAN Conference on Programming Language Design and Implementation, Seattle, Washington, USA, Jun. 2013, pp. 519-530.
- [36] J. Meng, A. Atle, H. Calandra, and M. Araya-Polo, "Minimod: A Finite Difference solver for Seismic Modeling," Jul. 2020, Accessed: Aug. 15, 2020. [Online]. Available: <https://arxiv.org/abs/2007.06048v1>.
- [37] D. Komatitsch, J. Tromp, "A perfectly matched layer absorbing boundary condition for the second-order seismic wave equation," *Geophysical Journal International*, volume 154, number 1, pp. 146-153, July 2003.
- [38] S. Williams, A. Waterman, and D. Patterson, "Roofline: an insightful visual performance model for multicore architectures," *Commun. ACM*, vol. 52, no. 4, pp. 65-76, Apr. 2009.
- [39] N. Ding and S. Williams, "An Instruction Roofline Model for GPUs," in 2019 IEEE/ACM Performance Modeling, Benchmarking and Simulation of High Performance Computer Systems (PMBS), Nov. 2019, pp. 7-18.
- [40] C. Yang, "Hierarchical Roofline Analysis on GPUs," ECP Annual Meeting, February 2020.
- [41] J. Mellor-Crummey, R. Fowler, and D. Whalley, "Tools for application-oriented performance tuning," in Proceedings of the 15th international conference on Supercomputing, Sorrento, Italy, Jun. 2001, pp. 154-165.
- [42] K. Zhou, M. Krentel, and J. Mellor-Crummey, "A tool for top-down performance analysis of GPU-accelerated applications," in Proceedings of the 25th ACM SIGPLAN Symposium on Principles and Practice of Parallel Programming, San Diego, California, Feb. 2020, pp. 415-416.
- [43] NVIDIA, "NVIDIA Tesla V100 GPU Architecture," August 2017.